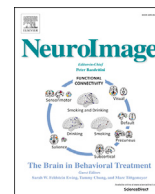




Contents lists available at ScienceDirect

NeuroImage

journal homepage: www.elsevier.com/locate/neuroimage

MR-guided joint reconstruction of activity and attenuation in brain PET-MR

Abolfazl Mehranian^{a,*}, Habib Zaidi^{b,c,d,e}, Andrew J. Reader^a^a Division of Imaging Sciences and Biomedical Engineering, Department of Biomedical Engineering, King's College London, St. Thomas' Hospital, London, UK^b Division of Nuclear Medicine and Molecular Imaging, Geneva University Hospital, CH-1211, Geneva, Switzerland^c Geneva Neuroscience Center, Geneva University, 1205, Geneva, Switzerland^d Department of Nuclear Medicine and Molecular Imaging, University of Groningen, University Medical Center Groningen, 9700 RB, Groningen, Netherlands^e Department of Nuclear Medicine, University of Southern Denmark, 500, Odense, Denmark

ARTICLE INFO

Keywords:

PET-MR

Brain imaging

Quantification

Attenuation correction

Segmentation

ABSTRACT

With the advent of time-of-flight (TOF) PET scanners, joint maximum-likelihood reconstruction of activity and attenuation (MLAA) maps has recently regained attention for the estimation of PET attenuation maps from emission data. However, the estimated attenuation and activity maps are scaled by unknown scaling factors. We recently demonstrated that in hybrid PET-MR, the scaling issue of this algorithm can be effectively addressed by imposing MR spatial constraints on the estimation of attenuation maps using a penalized MLAA (P-MLAA⁺) algorithm. With the advent of simultaneous PET-MR systems, MRI-guided PET image reconstruction has also gained attention for improving the quantitative accuracy of PET images, usually degraded by noise and partial volume effects. The aim of this study is therefore to increase the benefits of MRI information for improving the quantitative accuracy of PET images by exploiting MRI-based anatomical penalty functions to guide the reconstruction of both activity and attenuation maps during their joint estimation. We employed an anato-functional joint entropy penalty function for the reconstruction of activity and an anatomical quadratic penalty function for the reconstruction of attenuation. The resulting algorithm was referred to as P-MLAA⁺⁺ since it exploits both activity and attenuation penalty functions. The performance of the P-MLAA algorithms were compared with MLAA and the widely used activity reconstruction algorithms such as maximum likelihood expectation maximization (MLEM) and penalized MLEM (P-MLEM) both corrected for attenuation using a conventional MRI segmentation-based attenuation correction (MRAC) method. The studied methods were evaluated using simulations and clinical studies taking the PET image reconstructed using reference CT-based attenuation maps as a reference. The simulation results showed that the proposed method can notably improve the visual quality of the PET images by reducing noise while preserving structural boundaries and at the same time improving the quantitative accuracy of the PET images. Our clinical reconstruction results showed that the MLEM-MRAC, P-MLEM-MRAC, MLAA, P-MLAA⁺ and P-MLAA⁺⁺ algorithms result in, on average, quantification errors of $-13.5 \pm 3.1\%$, $-13.4 \pm 3.1\%$, $-2.0 \pm 6.5\%$, $-3.0 \pm 3.5\%$ and $-4.2 \pm 3.6\%$, respectively, in different regions of the brain. In conclusion, whilst the P-MLAA⁺ algorithm showed the best overall quantification performance, the proposed P-MLAA⁺⁺ algorithm provided simultaneous partial volume and attenuation corrections with only a minor compromise of PET quantification.

1. Introduction

Following the successful combination of positron emission tomography (PET) and x-ray computed tomography (CT), integrated PET and magnetic resonance imaging (MRI) has recently been introduced in clinical practice to further increase the advantages of multimodality imaging, since MRI provides superior soft tissue contrast and complementary functional information to PET molecular imaging data

compared to CT. Moreover, the quantitative accuracy of PET images, usually degraded by noise, partial volume effect (PVE) and motion blurring, can be improved by using MRI anatomical and motion-tracking information (Zaidi and Becker, 2016). In addition, the MRI does not impose additional radiation dose to the patient, which is of high importance in follow-up and paediatric imaging. However, the added benefits of combined PET-MR scanners come with the challenges of mutual compatibility of PET and MRI subsystems and the attenuation

* Corresponding author. Division of Imaging Sciences & Biomedical Engineering, King's College London, 3rd Floor, Lambeth Wing, St Thomas' Hospital, SE1 7EH, London, UK.
E-mail address: Abolfazl.Mehranian@kcl.ac.uk (A. Mehranian).

<http://dx.doi.org/10.1016/j.neuroimage.2017.09.006>

Received 19 June 2017; Received in revised form 21 August 2017; Accepted 4 September 2017

correction (AC) of PET data.

With the advent of avalanche photodiodes (APDs), the mutual incompatibility of PET and MRI systems has now been reasonably addressed (Delso et al., 2011) and even fully integrated time-of-flight (TOF) PET-MR scanners have been introduced thanks to fast silicon photomultipliers (SiPMs) (Levin et al., 2016). However, PET attenuation correction in PET-MR systems has still remained a challenge. In these systems, attenuation maps should ideally be derived from MR images, however, the conversion of MR image intensities to PET attenuation values is not as straightforward as in CT images, as they reflect the proton density and magnetic relaxation times of tissues rather than their photon attenuating properties. In addition, tissues with low proton density and short transverse relaxation (T2) times such as air and bone cannot be simply differentiated using clinically feasible MRI sequences. Hence, a number of different attenuation map generation methods has been proposed (Ladefoged et al., 2016; Mehranian et al., 2016b), including: MR-segmentation methods (Martinez-Möller et al., 2009; Zaidi et al., 2003), atlas-based and machine learning methods (Arabi and Zaidi, 2016; Burgos et al., 2014a) and emission-based methods (Salomon et al., 2011). In current PET-MR scanners, segmentation methods are the most widely used AC methods that aim to segment the MR images into a number of tissue classes (i.e. air, soft tissue, fat tissue, lungs and if possible bones) and to assign representative PET attenuation values to each class. In brain imaging, dedicated MRI sequences such as ultra-short and zero echo time (U/ZTE) have been developed to segment and include bones in the generated attenuation maps (Keereeman et al., 2010; Wiesinger et al., 2016). Currently, the Siemens APD-based PET-MR (mMR) scanner provides an optional dual UTE MR sequence for bone segmentation, however, these sequences are too time-consuming to be used in the clinic (around 4 min for the brain) but can provide high quality images enabling accurate and artefact-free bone segmentation (Aasheim et al., 2015). The atlas-based methods aim at generating a pseudo CT image by registration of multiple MR-CT pairs (atlas) to the subject's MR image and predict CT Hounsfield units using a variety of methods ranging from a simple averaging of the registered CT images to patch-based Gaussian regression methods (Hofmann et al., 2011). These AC methods have shown promising results in brain PET attenuation correction, since atlas registration is fairly accurate for the brain compared to whole body. Hence, the GE SiPM-based TOF PET-MR (SIGNA) scanner has implemented a clinical atlas-based AC method for brain PET-MR scans (Sekine et al., 2016a). The success of these methods however may depend on the employed atlas, in terms of the number, age group and gender of included MR-CT pairs, hence the SIGNA scanner also provides an optional ZTE-based bone segmentation method (Sekine et al., 2016b). Following the rebirth of TOF PET technology, the emission-based AC methods has regained popularity for the estimation of attenuation maps from PET emission data using the maximum likelihood reconstruction of activity and attenuation (MLAA) algorithm (Rezaei et al., 2012). These AC methods are especially promising for PET-MR systems where the employed attenuation maps are not patient specific (e.g. in the presence of metallic implants (Mehranian et al., 2016b)). However, both experimental and theoretical studies have shown that the MLAA reconstructed attenuation and activity maps suffer from an unknown scaling factor (Defrise et al., 2012). Nonetheless in PET-MR imaging, we previously demonstrated this scaling issue can be effectively addressed using MR-constrained Gaussian penalty functions (Mehranian and Zaidi, 2015b), which can facilitate the application of these new AC methods in clinical practice (Mehranian and Zaidi, 2015a).

With the advent of simultaneous PET-MR systems, the maximum a posteriori (MAP) and penalized maximum likelihood (PML) reconstruction of PET images using MRI anatomical penalty functions has also gained attention to reduce noise and PVE and therefore to improve the quantitative accuracy of the PET images (Bai et al., 2013). These reconstruction-based techniques, such as Bowsher's algorithm (Bowsher et al., 2004) aim at smoothing the PET images while preserving their valid boundaries based on a co-registered MRI anatomical image. Despite

promising results (Vunckx et al., 2012), these reconstruction-based methods have not gained wide acceptance, largely because of their vulnerability to mismatches between the anatomical image and the true activity distribution, which can induce false or suppress true PET features. Recently, we proposed a modified local joint-entropy penalty function that copes with the issue by relying on both PET and MRI information and therefore outperforms Bowsher's method in edge enhancement and preserving PET unique features (Mehranian et al., 2017).

Given the increasing prevalence of PET-MR imaging, the aim of this study is thus to maximize the benefits of MRI information in improving the quantitative accuracy of PET images by exploiting MR-based anatomical penalty functions to jointly guide the reconstruction of activity and attenuation maps during a penalized maximum likelihood reconstruction of activity and attenuation (P-MLAA) algorithm. As a result, not only are the PET images corrected for attenuation more accurately but also they are corrected for PVE. In this study, the performance of the proposed P-MLAA was extensively evaluated using realistic simulation and clinical imaging datasets. The emission-based and atlas-based AC methods have been previously compared in (Mehranian et al., 2016a) and (Ladefoged et al., 2016), therefore in this work we aimed to highlight the increased benefits of MR information in the joint reconstruction of activity and attenuation images.

2. Material and methods

2.1. Reconstruction of activity and attenuation maps

In the joint reconstruction framework, the PET activity (λ) and attenuation (μ) maps are jointly estimated by maximizing the penalized log-likelihood of the λ and μ given the TOF PET measured data (y) as follows:

$$(\hat{\lambda}, \hat{\mu}) = \underset{\lambda, \mu}{\operatorname{argmax}} \left\{ \sum_{i=1}^M \sum_{t=1}^T \log p(y_{it} | \lambda, \mu) + \beta R(\lambda) + \gamma X(\mu) \right\} \quad (1)$$

where the probability distribution $p(y_{it} | \lambda, \mu)$ of the measured data value in the i th sinogram bin (line of response –LOR) and the t th TOF bin is modelled using the Poisson distribution with an expected value of

$$\mathbb{E}[y_{it}] = n_i \exp \left(- \sum_{j=1}^N l_{ij} \mu_j \right) \sum_{j=1}^N g_{ijt} \lambda_j + \bar{r}_{it} + n_i \bar{s}_{it} \quad (2)$$

where n_i is the detector normalization factor of the i th LOR, l_{ij} is the intersection length of the i th LOR and the j th voxel, the exponential term accounts for photon attenuation along the i th LOR, g_{ijt} is the geometric probability detection of annihilation events emitted from the j th voxel along the i th LOR in t th TOF bin, \bar{r}_{it} and \bar{s}_{it} are the expected number of randoms and scatter coincidences in the (i, t) th sinogram bin, respectively obtained using a delayed coincidence window and model-based single scatter simulation. $R(\lambda)$ and $X(\mu)$ are penalty functions used to impose the MR-derived prior knowledge about activity and attenuation maps. The PET images reconstructed using the standard maximum-likelihood expectation maximization (MLEM) are usually contaminated with noise, especially in low-dose or short-time scans. As a result, in clinical practice the reconstructed images are routinely smoothed using a Gaussian kernel, which notably reduces noise but at the expense of deteriorating image resolution and increasing the PVE. The penalty function $R(\lambda)$ is therefore designed such that it suppresses noise in PET activity images, based on the local differences between neighbouring voxels, but it preserves valid boundaries and even recovers lost features, based on an anatomical MR image. In this study, we used an anatomical functional penalty function for activity images, derived from the local approximation of the joint Burg entropy (Mehranian et al., 2017). This penalty function can be described using its partial derivative as follows

(see Appendix A for more details):

$$\frac{\partial R(\lambda)}{\partial \lambda_j} = -2 \sum_{b \in \mathcal{N}_j} \xi_{jb} \omega_{jb} (\lambda_j - \lambda_b),$$

$$\omega_{jb} = \frac{\mathcal{G}(\lambda_j, \lambda_b, \sigma_\lambda) \mathcal{G}(\theta_j, \theta_b, \sigma_\theta)}{\sum_{b \in \mathcal{N}_j} \mathcal{G}(\lambda_j, \lambda_b, \sigma_\lambda) \mathcal{G}(\theta_j, \theta_b, \sigma_\theta)}, \quad \mathcal{G}(q, r, \sigma) = \frac{1}{\sqrt{2\pi}\sigma} \exp\left(-\frac{(q-r)^2}{2\sigma^2}\right).$$
(3)

where \mathcal{N}_j is a neighbourhood around the j th voxel in which the intensity differences between voxels j and b are calculated, ξ_{jb} and ω_{jb} are the coefficients that weight the intensity differences based on their proximity and similarity, respectively. In this study, the proximity coefficients were defined as the inverse of the Euclidean distance between the j th and b th voxels. The similarity coefficients are derived from the joint probability distribution (PDF) of the PET image (λ) and the MRI anatomical image (θ). The joint PDF is approximated using the Parzen density estimation with a bivariate Gaussian (\mathcal{G}) window function with standard deviations (bandwidths) of σ_λ and σ_θ . The role of ω_{jb} is to assign lower weights or penalty on the local differences that are associated with a boundary identified uniquely from the PET image or commonly from both PET and MRI images. In PET unique boundaries, the MR-derived Gaussian kernels in ω_{jb} are uniform, whereas in shared boundaries they have the same structural similarity as in PET-derived kernels, irrespective of image contrast and signal intensity. Therefore, the multiplication of the kernels will preserve the PET unique boundaries and encourage the formation of shared ones.

For the attenuation map the following spatially constrained log-Gaussian penalty function was employed:

$$X(\mu) = \sum_{j \in S} \log \mathcal{G}(\mu_j, \bar{\mu}_s, \sigma_s) \quad (4)$$

where S is the set of soft tissue voxels identified from the segmentation of an MRI anatomical image $\bar{\mu}_s$ and σ_s are the expected value and standard deviation of attenuation coefficients of the soft tissue class. This penalty function penalizes particularly large deviations of the estimated soft tissue attenuation values from their expected value, as a result, the noise and cross-talk artifacts are substantially suppressed and the scaling issue of the joint reconstruction is effectively solved. By this penalty function, the attenuation estimation of other tissue classes that do not have signal intensity in the MR images such as bone and internal air cavities remains unconstrained.

2.1.1. Optimization

The simultaneous maximization of the problem in (1) is not straightforward, hence an alternating optimization is performed by maximization with respect to λ while keeping μ constant and vice versa (Rezaei et al., 2012). The PET and attenuation optimization steps were respectively solved using P-MLEM with Green's one step late (OSL) (Green, 1990) and a penalized maximum likelihood transmission tomography (P-MLTR) algorithm. The algorithm repeats the steps defined in Eqs. (5–8).

$$a_i^n = \exp\left(-\sum_j l_{ij} \mu_j^n\right) \quad (5)$$

$$\lambda_j^{n+1} = \frac{\lambda_j^n}{\sum_i g_{ij} n_i a_i^n + \beta \frac{\partial R(\lambda^n)}{\partial \lambda_j}} \sum_i \sum_t n_i a_i^n g_{ijt} \frac{y_{it}}{n_i a_i^n \sum_k g_{ikt} \lambda_k^n + \bar{b}_i} \quad (6)$$

$$\psi_i^n = n_i a_i^n \sum_j g_{ij} \lambda_j^{n+1} \quad (7)$$

$$\mu_j^{n+1} = \left[\mu_j^n + \alpha \left(\frac{\sum_i l_{ij} \frac{\psi_i^n}{\psi_i^n + \bar{b}_i} (\psi_i^n + \bar{b}_i - y_i) - \gamma \frac{\mu_j^n - \bar{\mu}_s}{\sigma_s^2}}{\sum_j l_{ij} \frac{(\psi_i^n)^2}{\psi_i^n + \bar{b}_i} \sum_k l_{ik} - \frac{\gamma}{\sigma_s^2}} \right) \right]_+ \quad (8)$$

where $\bar{b}_{it} = \bar{r}_{it} + n_i \bar{s}_{it}$ is the expected value of the background coincidences in the (i, t) th sinogram bin, $g_{ij} = \sum_t g_{ijt}$, $y_i = \sum_t y_{it}$ and $\bar{b}_i = \sum_t \bar{b}_{it}$ are TOF-integrated quantities and $\alpha > 0$ is a step size parameter.

Three constraints were used for the estimation of the attenuation coefficients: i) a non-negativity constraint, $[\]_+$, which sets negative values to zero, ii) a background constraint to impose background air attenuation coefficients and iii) insertion of the patient couch attenuation coefficients. In (5), the attenuation factors are calculated from a current μ -map and are used for the reconstruction of activity in (6) using a TOF OSL-P-MLEM algorithm. Then in (7), the current estimate of the mean emission data sinograms is calculated from the current activity estimate, but without background coincidences. Finally, the attenuation map is reconstructed using a P-MLTR algorithm in (8). In the case of having no penalty function on attenuation estimation (i.e. $\gamma = 0$) the P-MLTR algorithm becomes the maximum likelihood transmission tomography (MLTR). The attenuation reconstruction was initialized using the MR segmentation-based attenuation map used currently in clinical practice (see the next section for details), while the activity reconstruction was initialized by a uniform map.

In this study, several reconstruction methods were evaluated including i) the conventional MLEM PET image reconstruction using CT-derived attenuation maps (CTAC) and MR-segmentation based attenuation maps (MRAC), hereafter referred to as MLEM-CTAC and MLEM-MRAC, ii) the MR-guided P-MLEM PET image reconstruction using CTAC and MRAC methods, hereafter, P-MLEM-CTAC and P-MLEM-MRAC, iii) the MLAA algorithm, iv) the proposed P-MLAA algorithm using MRI information to improve the attenuation estimation, hereafter P-MLAA⁺, and to improve both PET image reconstruction and attenuation estimation, hereafter, P-MLAA⁺⁺. The proposed activity penalty function $R(\lambda)$ was used for both P-MLAA⁺ and P-MLAA⁺⁺ reconstruction. The PET images reconstructed using MLEM-CTAC were used as a reference for those reconstructed using the MLEM-MRAC, MLAA and the P-MLAA⁺ algorithms, whereas the PET images reconstructed using P-MLEM-CTAC were considered as the reference for the PET images of the P-MLEM-MRAC and P-MLAA⁺⁺ algorithms. Table 1 further summarizes the list of the considered reconstruction and attenuation correction methods together with their reference methods. The performance of these reconstruction methods was extensively evaluated using 3D realistic simulations and clinical datasets, as described in the following sections.

2.2. Simulations and clinical PET/MR/CT data

2.2.1. Numerical simulations

To quantitatively evaluate the performance of the reconstruction

Table 1

List of the reconstruction and attenuation correction methods considered in this study together with their reference method.

Reference	MLEM-CTAC	P-MLEM-CTAC
Methods	MLEM-MRAC MLAA P-MLAA ⁺	P-MLEM-MRAC P-MLAA ⁺⁺

MLEM: Maximum likelihood expectation maximization.

P-MLEM: Penalized MLEM with an activity penalty function.

MLAA: Maximum likelihood reconstruction of activity and attenuation.

P-MLAA⁺: Penalized MLAA with an attenuation penalty function.

P-MLAA⁺⁺: Penalized MLAA with attenuation and activity penalty functions.

CTAC: CT-based attenuation correction.

MRAC: MR-segmentation based attenuation correction.

methods with respect to a ground truth, realistic analytical simulations were performed using a brain phantom obtained from the BrainWeb phantom (Cocosco et al., 1997) and a model of the geometry of the Siemens PET/CT (mCT) scanner with TOF capability. As shown in Fig. 1, the brain phantom was simulated as an [^{18}F]fluorodeoxyglucose (FDG) PET scan with 3 to 1 mean activity concentration ratio in grey matter (GM) to white matter (WM). The figure also shows the corresponding T1-MR, CTAC (true) and MRAC attenuation maps. To simulate the functional and anatomical inconsistencies between PET and MR images, two PET unique lesions were introduced in the true activity images (see arrows in Fig. 1). In addition, a few regions of the brain were uniquely removed from the MR image. To simulate PVE and noise in the MR image, the simulated MRI phantom was smoothed using a Gaussian kernel, 3 mm full width at half maximum (FWHM) and contaminated by Gaussian noise with standard deviation equal to 1% of the largest voxel intensity. The true attenuation map consists of air, soft tissue and bone tissue classes, with linear attenuation coefficients (μ) of 0, 0.098 and 0.13 cm^{-1} , respectively, while the MR-derived attenuation map consists of the air and soft tissue classes with μ -value of 0 and 0.096 cm^{-1} , respectively. Note that it was assumed that the μ assigned to the soft tissue of the MRAC map is not patient-specific and slightly different from the true μ of soft tissue. The true attenuation was derived from a high-resolution anatomically segmented model provided in the BrainWeb phantom. An attenuation coefficient of 0.098 cm^{-1} was assigned to soft tissue structures (such as grey matter, white matter, CSF, vessels, muscles, fat, and so on), an attenuation coefficient of 0.13 cm^{-1} was assigned to bony structures (such as dura matter, skull) whereas 0 cm^{-1} was assigned to air cavities and background air. The field of view (FOV) and matrix size of the resulting high-resolution phantom was modified by zero-padding and down sampling of the phantom to the FOV and matrix size of the mCT scanner.

The 3D simulations were performed for the mCT scanner with the following specifications: 4 block rings of 32448 crystals with dimensions of $4 \times 4 \times 20\text{ mm}^3$, effective detector radius of 437.2 mm, coincidence window width of 4.06 ns with a nominal TOF timing resolution of 580 ps and the sinogram size of 400 radial bins, 168 angular projections, 621 sinogram planes (in 9 segments with span 11) and 13 TOF bins. The CT subsystem is a 128-slice CT scanner (SOMATOM Definition AS+) with an extended transaxial FOV of 780 mm. Due to the high reconstruction time of TOF data, particularly over multiple noise realization used for bias variance analysis (see next section), for our simulations only 3 segments were considered, leading to sinograms of 303 planes, which reduced the reconstruction time by 50%. The prompt emission sinograms were obtained by the attenuated and normalized TOF forward projection of the true activity and were contaminated with simulated TOF randoms and scatter coincidences. The attenuation factors were obtained by the non-TOF forward projection of the true attenuation map. The normalization

factors were simulated by a 5% random fluctuation of detector efficiency. The scatter sinograms were simulated by smoothing of the emission sinograms of segment zero (direct planes) in the radial, angular, and TOF directions with a Gaussian kernel of 20 cm, 8 radians, 660 ps FWHM, respectively. The simulated 2D scatter sinograms were then extended to 3D sinograms using inverse single slice rebinning (iSSRB). The randoms sinograms were simulated as Poisson noise with a constant mean value. In our simulations, a 100 million count PET scan with scatter and randoms fractions of 10% and 35% were considered.

2.2.2. PET/CT and MRI data acquisition

In this study, the PET/CT and MRI brain datasets of 8 patients, scanned at Geneva University Hospital, were employed for the performance evaluation of the MLEM-MRAC, MLAA and P-MLAA⁺ reconstruction methods with respect to their reference MLEM-CTAC method and that of the P-MLEM-MRAC and P-MLAA⁺⁺ with respect to their reference P-MLEM-CTAC method. The patients were referred for FDG PET imaging with clinical indications of epilepsy and dementia and scanned 20 min after injection of $210.2 \pm 13.9\text{ MBq}$ [^{18}F]FDG. A low-dose CT-scan was also performed for the CT-based attenuation correction of PET data with 120 kV_p and 20 mAs. The patients also underwent diagnostic MR imaging on a 3T Siemens MAGNETOM Skyra scanner. The MRI scans included a 3D T1-weighted magnetization prepared rapid gradient-echo, MPRAGE (TE/TR/TI, 2.3 ms/1900 ms/970 ms, flip angle 8°, NEX = 1, voxel size $0.8 \times 0.8 \times 0.8\text{ mm}^3$) and a multi-slice 2D T2-weighted turbo spin-echo, TSE (TE/TR, 100 ms/6200 ms, NEX = 2, voxel size $0.4 \times 0.4 \times 4\text{ mm}^3$). The study was approved by the institutional review boards and the research ethics committee. Written informed consent was obtained from all study participants.

2.3. Attenuation map generation and image reconstruction

For each clinical dataset, three types of attenuation map and two types of scatter sinograms were generated. The attenuation maps were obtained using CTAC, MRAC and emission-based methods and the scatter sinograms were estimated using single scatter simulation based on CTAC and MRAC maps. The CTAC maps were generated by converting the CT Hounsfield units to 511-keV attenuation coefficients using a kV_p-dependent bilinear mapping approach (Carney et al., 2006). The resulting high resolution continuous attenuation maps are then matched with the FOV of PET and downsized to a resolution of 400×400 with voxel size of $2.04 \times 2.04 \times 2.03\text{ mm}^3$. Finally, they were smoothed to the resolution of PET images using an isotropic Gaussian kernel (4 mm FWHM).

For the MR-based AC and MR-guided PET image reconstruction, the T1- and T2-weighted MR images of each patient were registered to the space of a previously reconstructed PET image using the Hermes

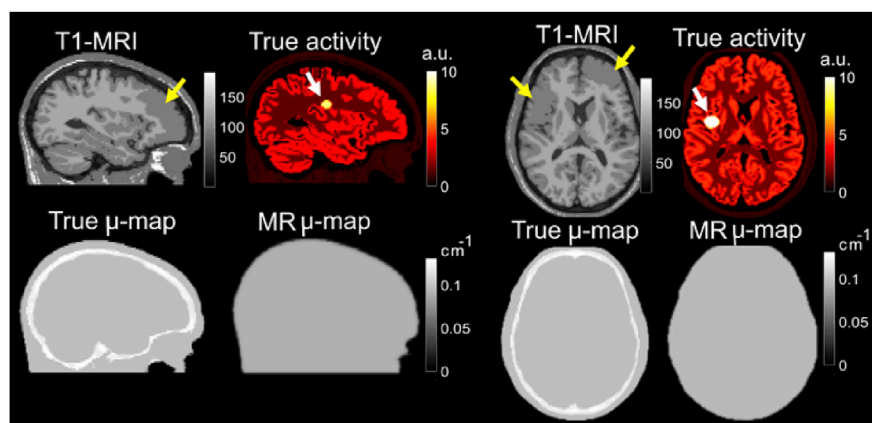


Figure 1. The FDG simulated brain phantom including the T1-weighted MR image and the true and MR-segmentation-based attenuation maps, shown in sagittal and transverse views. The arrows indicate the simulated functional and anatomical inconsistencies between PET and MR images.

multimodality brain registration software (Hermes medical solutions AB, Sweden). The normalized mutual information was used as a similarity metric and a multi-resolution method with a gradient descent optimizer was used for registration of MR to PET images. The CT images acquired on the mCT PET-CT scanner were already registered to the PET images. The resolution and FOV of the registered MR images were matched to their corresponding CT images using the Elastix registration tool (Klein et al., 2010). For MRAC, a two tissue class attenuation map including background air and soft tissue was considered. The T1-weighted MR images were segmented for soft tissue using a heuristically defined threshold. Water-containing tissues such as eyes and the brain's ventricles usually have long T1 and T2 relaxation times, which appear dark and bright in T1 and T2-weighted images, respectively. To include such tissues into the soft tissue class, the T2 MR images were used to complement the T1 images. Note that in both T1 and T2 images the tissues with short T2 relaxation time such as bones or low proton density such as air appear dark and without signal. The background air tissue class was segmented by thresholding of the reference CTAC images in order to reduce the mis-registration errors between MRAC and CTAC maps. The resulting background mask were slightly dilated using a morphological filtering operator to compensate for any under-segmentation raised by thresholding. For each patient, an additional unknown tissue class was then defined as the complement of the segmented soft tissue and background air, which included the regions of the MR images that were of low signal intensities such as bones, air cavities and susceptibility artifacts. To generate the two-class MRAC maps, the μ -values of 0, 0.0975 cm^{-1} and 0.0975 cm^{-1} were assigned to the background air, soft tissue and the unknown tissue classes, respectively. The resulting MRAC maps were then smoothed using a 4 mm Gaussian kernel. The Siemens e7 tools were used to generate TOF scatter sinograms using the CTAC and MRAC maps. The resulting segment-zero sinograms were extended to fully 3D sinograms using the iSSRB algorithm. The normalization and smoothed randoms sinograms were also generated using the Siemens e7 tools.

For the emission-based estimation of activity and attenuation using the MLAA algorithm and its MR-guided variants, the activity images, attenuation maps, attenuation factors and scatter sinograms were respectively initialized by a uniform matrix of ones, the MRAC maps, MRAC-derived attenuation factors and MRAC-based scatter sinograms. For the P-MLAA methods, the soft tissue set, S , of the penalty function defined in eq. (4) was set to the same as the one obtained from the segmentation of the MR images. The parameters of this penalty function were set to $\bar{\mu}_s = 0.0978 \text{ cm}^{-1}$ and $\sigma_s = 0.0015 \text{ cm}^{-1}$ for both simulations and clinical reconstructions. These parameters were calculated as the mean and standard deviation of soft tissue attenuation coefficients derived from the averaging of single CT-based soft tissue attenuation coefficients of a population of patients (14 brain scans). For each patient, the single soft tissue coefficients were obtained from averaging of the attenuation coefficients of all voxels in the soft tissue class. The emission-based reconstruction methods are composed of two reconstruction steps: i) activity reconstruction using MLEM or P-MLEM and ii) attenuation estimation using MLTR or P-MLTR algorithms. In all of our studied reconstructions of both simulations and clinical datasets, the following reconstruction parameters were used, number of global iterations: 100, number of MLEM/P-MLEM updates: 2, number of MLTR/P-MLTR updates: 3, $\alpha = 1$. For penalized reconstructions, the window size, \mathcal{N}_j , of the local joint entropy penalty function was set to $5 \times 5 \times 5$, for simulation the bandwidth parameters of the penalty function were set to $\sigma_\theta = 5$ and $\sigma_\lambda = 0.5$, while for clinical datasets, they were set to $\sigma_\theta = 5$ and $\sigma_\lambda = 1$. The regularization parameters of the activity and attenuation penalty functions were set to $\beta = 100$ and $\gamma = 0.025$ for simulations and $\beta = 1000$ and $\gamma = 0.1$ for the clinical imaging datasets.

2.4. Evaluation metrics

The quantitative performance and convergence properties of the

reconstruction methods were evaluated using the simulation. For this purpose, a region-of-interest (ROI) based bias-variance analysis was performed using 10 Poisson noise realizations. Three ROIs were defined from the true activity maps including: white matter (WM), grey matter (GM) and tumours. The normalized absolute bias in each ROI was calculated as:

$$\text{Bias} = 100 \times \frac{1}{N_{ROI}} \sum_{j \in ROI} \frac{|\bar{\lambda}_j - \lambda_j^{ref}|}{\lambda_j^{ref}} \quad (9)$$

where $\bar{\lambda}_j = \frac{1}{N_r} \sum_{r=1}^{N_r} \lambda_j^r$ represents the ensemble mean value of each voxel calculated for all N_r noise realizations. N_{ROI} is the total number of voxels in the ROI. λ_j^{ref} is a reference PET (or ground truth) image. For simulations, the true activity was considered as reference PET image, while for the clinical studies, PET images corrected using CTAC attenuation maps were considered as reference images. The variance was calculated using the average of the pixel-level coefficient of variation (COV) for each ROI:

$$\text{COV} = 100 \times \frac{1}{N_{ROI}} \sum_{j \in ROI} \frac{\sqrt{\frac{1}{N_r} \sum_{r=1}^{N_r} (\lambda_j^r - \bar{\lambda}_j)^2}}{\bar{\lambda}_j} \quad (10)$$

For the clinical datasets and a single noise realization of simulation data, the quantitative performance of the algorithms was evaluated using the following relative quantification error in the estimated activity in a given ROI:

$$\text{Error} = 100 \times \frac{1}{N_{ROI}} \sum_{j \in ROI} \frac{\lambda_j - \lambda_j^{ref}}{\lambda_j^{ref}} \quad (11)$$

For simulations, the same GM, WM and tumour regions were used, while for each of the clinical datasets, 14 circular volumes of interest (VOIs) were defined on different regions of the brain using the co-registered T1-weighted MR images. The VOIs included frontal, temporal and occipital lobes, cerebrum, caudate nucleus, thalamus, putamen and brain stem. The correlation between the reconstructed activity images using the MLEM-MRAC, MLAA and P-MLAA+ and their reference MLEM-CTAC images and between those reconstructed by P-MLEM-MRAC and P-MLAA++ and their reference P-MLEM-CTAC images were using scatter plots.

3. Results

3.1. Simulations

Fig. 2 compares the activity and attenuation maps of the brain phantoms reconstructed/derived using different methods together with their reference maps. The activity and attenuation profiles also compare the performance of the algorithms along the dashed lines. The PET images reconstructed using the MLEM, MLAA and P-MLAA+ algorithms have been smoothed using an isotropic Gaussian smoothing with 4 mm FWHM. The results show that the un-regularized reconstructions at the top of the figure suffer from noise and PVE and therefore deviate from the piece-wise smooth true activity image. However, the PET images reconstructed using the P-MLEM and P-MLAA++ algorithms show reduced noise and enhanced boundaries, as these algorithms exploit the MRI anatomical information using the local joint Burg entropy function in Eq. (3). By design of the simulation, the T1-weighted MR image has both functional and anatomical mismatches compared to the true PET image, in terms of the tumour and frontal lobe region of the brain. Despite these mismatches, the employed penalty function is able to address them compared with the conventional anatomical penalty functions that suppress the tumour and induce pseudo edges in the PET images.

The results of the attenuation map estimation from emission data also

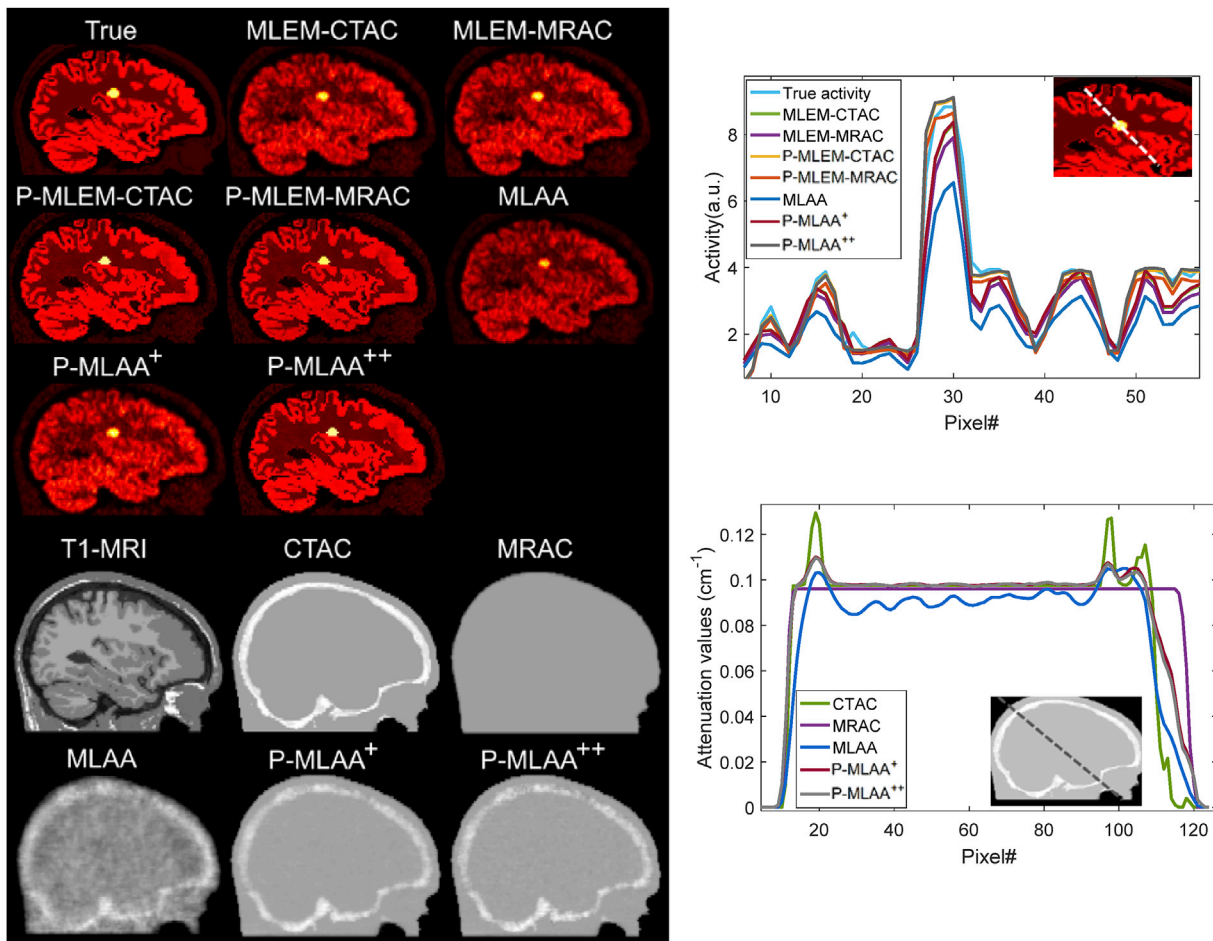


Figure 2. The reconstruction results of the brain phantom. Top: the activity maps estimated using different reconstruction and attenuation correction methods. Bottom: T1-weighted MRI and reference CTAC and different attenuation maps estimated using MRI-segmentation and emission-based methods. The activity and attenuation maps are shown in the same display windows as in Fig. 1.

show that the MLAA, P-MLAA⁺ and P-MLAA⁺⁺ algorithms can estimate the bone tissues, which are missing in the MRAC maps, however, as can be seen, the attenuation values of soft tissue have been underestimated using the MLAA algorithm, which can be attributed to the scaling issue and therefore instability of the algorithm. Whereas the P-MLAA algorithms exploit MR-derived soft tissue constraints using the penalty function in Eq. (4). The profiles also show that the MLAA algorithm results in underestimation of soft tissue μ_s , which in turn gives rise to under-correction and underestimation of the tumour's estimated activity. The activity profiles show that the MLEM-MRAC algorithm also leads to underestimation of true activity as in the employed attenuation maps, bone tissue is replaced by soft tissue. It is also noticeable that the attenuation map of the P-MLAA⁺⁺ algorithm is slightly noisier than that reconstructed by the P-MLAA⁺ algorithm. The reason is that in P-MLAA⁺⁺ the MRI information is used to suppress noise in the activity image. This means that the difference between the calculated and measured projection data in Eq (8) will in fact contain greater noise, which in turn manifests in the reconstructed attenuation maps. In the [supplementary material Fig. 1](#), the reconstructed images have been further compared in coronal views. Fig. 3 (left column) shows the performance of the algorithms in terms of quantification errors with respect to the true activity, defined in Eq. (11), as a function of iteration number for the GM, WM and tumour regions of the brain phantom.

The results show that the MLAA algorithm and the PET images corrected using the MRAC method show the highest quantification errors, whereas those reconstructed by the P-MLAA and MLEM/P-MLEM-CTAC algorithms show the least errors. These results were calculated for a

single noise realization. The bias-variance performance of the algorithm over 10 noise realizations is shown in Fig. 3 (right column) for the three regions of interest. As can be seen for the high-activity regions such as the GM and tumours, with increasing iteration number, the bias of the estimated activity in the ROIs is reduced, while the variance (COV) is increased in the case of un-regularized reconstruction methods. In the WM region, after a certain number of iterations the bias is not reduced but rather increases, which can be attributed to the bias due to noise in such low-uptake regions of the FDG PET scans. It is noticeable that the bias-variance curves of the P-MLAA⁺ and P-MLAA⁺⁺ algorithms eventually approach to their reference curves of the MLEM-CTAC and P-MLEM-CTAC algorithm, especially in the GM and WM regions. Overall, these simulation results show that the proposed P-MLAA⁺⁺ algorithm exploits the MRI information to improve the PET image by simultaneous attenuation and PVE correction (less bias) and it approaches the best performing P-MLEM-CTAC algorithm.

3.2. Clinical studies

Figs. 4 and 5 show the reconstruction results of two representative clinical datasets. The un-regularized PET reconstructions were post-smoothed using a 4-mm FWHM Gaussian kernel. The unfiltered MLEM-CTAC PET images have also been shown to highlight the importance of smoothing or regularization especially when the PET images are reconstructed using a high number of iterations of the MLEM-type algorithms. Note the P-MLEM-MRAC results have not been shown in these figures. The results show that the inclusion of MRI anatomical information into

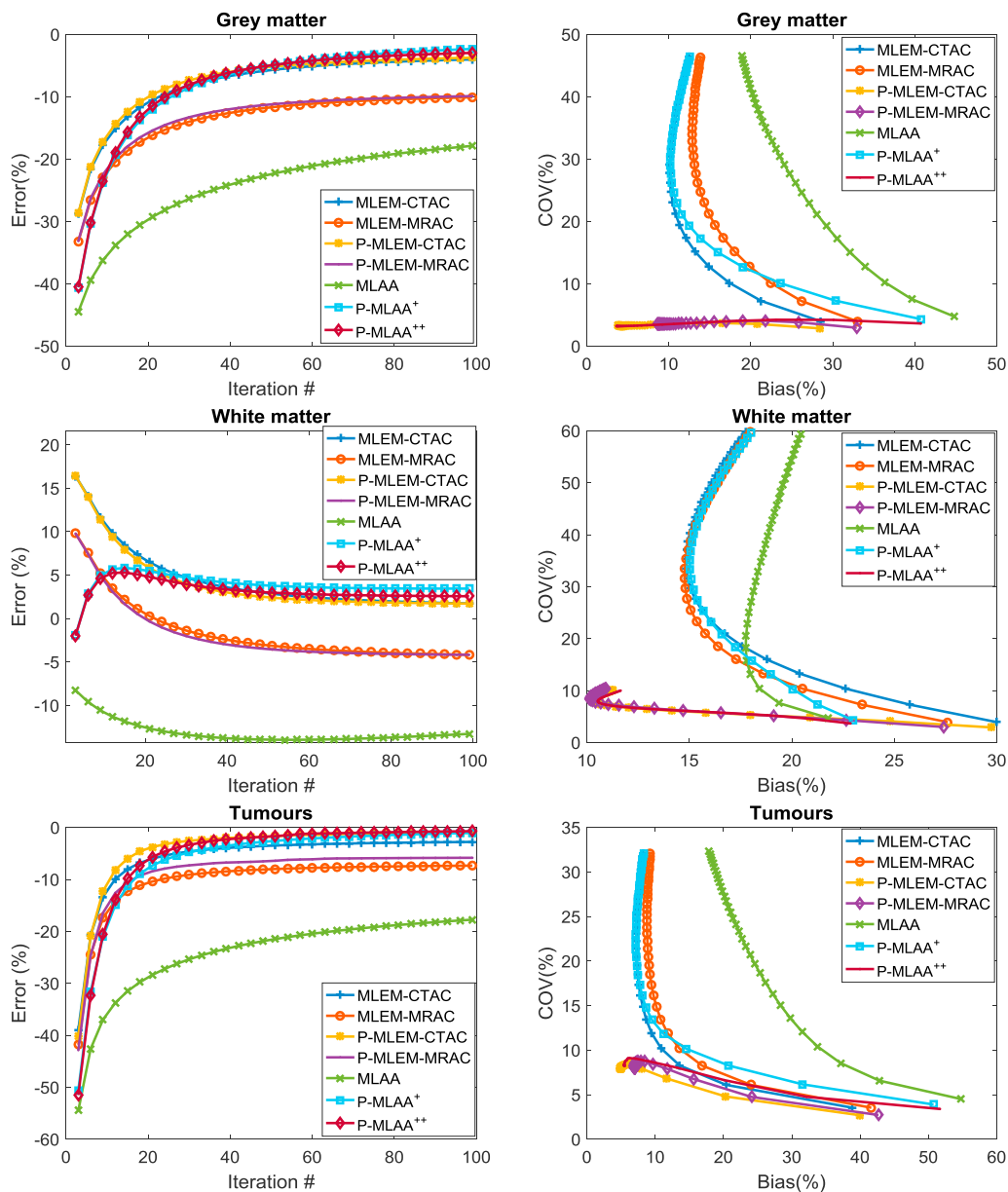


Figure 3. Left column: The quantification errors of the activity reconstructed with the studied methods as a function of iteration for different regions of the brain, for a single noise realization. Right column: bias-variance analysis of the methods for 10 noise realizations.

PET image reconstruction can not only suppress noise and PVE but also recover some details that cannot be recovered from PET data due to the intrinsically limited resolution of PET scanner.

The attenuation maps reconstructed by the MLAA algorithm show noise and slightly over-estimated attenuation values in soft tissue regions of the brain, while those reconstructed by the P-MLAA algorithms are closer to the reference CTAC maps. Nonetheless, the MLAA algorithm has well recovered air cavities and bones. As a result, the MLAA and P-MLAA reconstructions achieve notably improved qualitative performance over the MLEM-MRAC algorithm (see their quantitative performance at the end of this section). [Supplemental Figs. 2 and 3](#) show the same results for two additional patients, where the P-MLAA++ algorithm consistently outperformed other algorithms in noise reduction and attenuation and PVE correction.

[Fig. 6](#) compares the attenuation maps obtained from the studied AC methods for the same dataset shown in [Fig. 4](#) in sagittal, transverse and coronal views with the reference CTAC and T1-weighted MR images. As shown, the emission-based AC methods can reasonably well estimate

bones and air cavities and thus improve upon the MR-segmentation based AC method that substitutes them with the μ -value of soft tissue. It is also noticeable that the performance of the emission-based AC methods depends on the count level, which is more pronounced at the bottom edge of the MLAA attenuation maps in the sagittal and coronal view. In fact, due to lower sensitivity of the scanner as the edges of the axial FOV, the emission data are noisier and therefore the estimated attenuation maps are noisier.

[Fig. 7](#) compares the mean attenuation values of air cavities, soft tissue and bones estimated by difference AC methods for the simulated brain phantom and the eight patient datasets. [Table 1](#) in the supplementary material provides mean and standard deviation of the attenuation values. The internal air, soft and bone tissue classes were obtained from the co-registered reference CTAC attenuation map using simple thresholding-based segmentation. For each patient, the patient's bed was removed using an interactive graphical interface and then background air was segmented using a threshold of 0.001 cm^{-1} subject to a hole filling operator. The bones and internal air cavities were segmented using

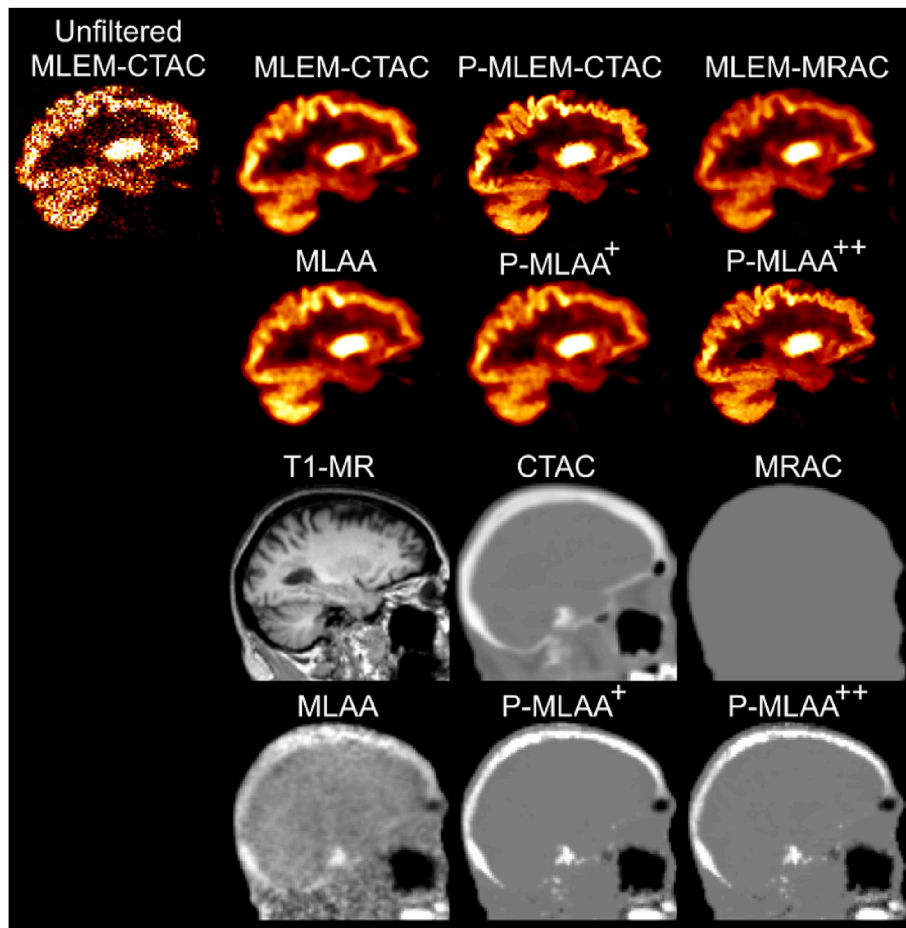


Figure 4. The reconstruction results of the studied reconstruction and attenuation estimation methods for an FDG brain PET scan. The PET images of the (P-)MLEM-CTAC, (P-)MLEM-MRAC, M-LAA and P-M-LAA algorithms are shown after smoothing using a 4-mm-FWHM Gaussian filter. The attenuation maps are also smoothed using the same filter.

thresholds of 0.03 and 0.11 cm^{-1} , respectively. Finally the soft tissue class was identified as a complement of the bone and air tissue classes. In the studied 2-class MRAC method, air cavities and bones were assigned with attenuation coefficients of soft tissue. The results show that all the emission-based AC methods overestimate the mean attenuation coefficients of air cavities in the considered patient. Note in the top graph of Fig. 7, the range of attenuation coefficients was set to level of 0.05 cm^{-1} . The results show that the M-LAA algorithm underestimates the soft tissue attenuation values in the brain phantom, while it overestimates them in all patient datasets. The P-M-LAA algorithms perform almost equally in the estimation of soft tissue μ -value with a slight overestimation of μ -values of the patients 5 onward. For all clinical datasets, the mean of soft tissue μ -values for the CTAC, MRAC, M-LAA, P-M-LAA⁺ and P-M-LAA⁺⁺ methods were 0.097 , 0.096 , 0.105 , 0.098 and 0.098 cm^{-1} , respectively. Note that the attenuation maps were smoothed using an isotropic 4 mm Gaussian filter, therefore the μ -values of MRAC method show some variations due to PVE at the air soft-tissue interfaces. The results for bone tissue show that the emission-based AC methods can well estimate bone μ -values compared to the MRAC method that ignores bones in the AC maps. However, in overall they slightly underestimate bones. For all clinical datasets, the mean of bone μ -value for the CTAC, MRAC, M-LAA, P-M-LAA⁺ and P-M-LAA⁺⁺ methods were 0.136 , 0.096 , 0.130 , 0.130 and 0.128 cm^{-1} , respectively.

The quantitative performance of the different reconstruction methods were compared with their reference method. As mentioned earlier, MLEM-CTAC was used as a reference for MLEM-MRAC, M-LAA and P-M-LAA⁺ methods, while the P-MLEM-CTAC was used as a reference for the P-MLEM-MRAC and P-M-LAA⁺⁺ methods. The reason is that the

incorporation of the MRI anatomical information modifies both noise and convergence properties of the reconstructed PET images, therefore it is advisable to use two Fig. 8 shows the voxel-wise error maps of the reconstructed PET images of the patient datasets shown in Figs. 4–5, calculated according to Eq. (11). The results show that the PET reconstructions with MR-based attenuation correction suffer from a substantial underestimation of tracer uptake especially in close vicinity of the bone. It is noticeable that the application of MRI anatomical penalty functions in the P-MLEM algorithms does not compensate for the tracer underestimations caused by inaccurate attenuation correction. The error map of the M-LAA algorithm shows that this algorithm results in some regional overestimation of the tracer uptake, due to overestimation of soft tissue attenuation values, whereas the P-M-LAA algorithms can notably reduce the errors. Again, the applied MRI anatomical penalty function in P-M-LAA⁺⁺ algorithm has no influence on error reduction. In Fig. 8.A, it is noticeable that the P-M-LAA algorithm, and to some degree the M-LAA algorithm, have resulted in positive errors in the vertex of the skull, which is due to overestimated bone attenuation coefficients, as show in Fig. 4. These errors are mainly due to the lower sensitivity of the PET scanner and count level at the edge of the axial FOV, which affect the performance of these emission-based AC methods.

Fig. 9 compares the quantitative performance of the algorithms in terms of the mean quantification errors in different regions of the brain among all 8 patients. Table 2 supplementary material also summarizes the mean and standard deviation of the errors in each region. The results show that the attenuation correction using the MRAC method results in a considerable error in most areas of the brain while the emission-based methods significantly reduce the errors by estimating bone μ -value and

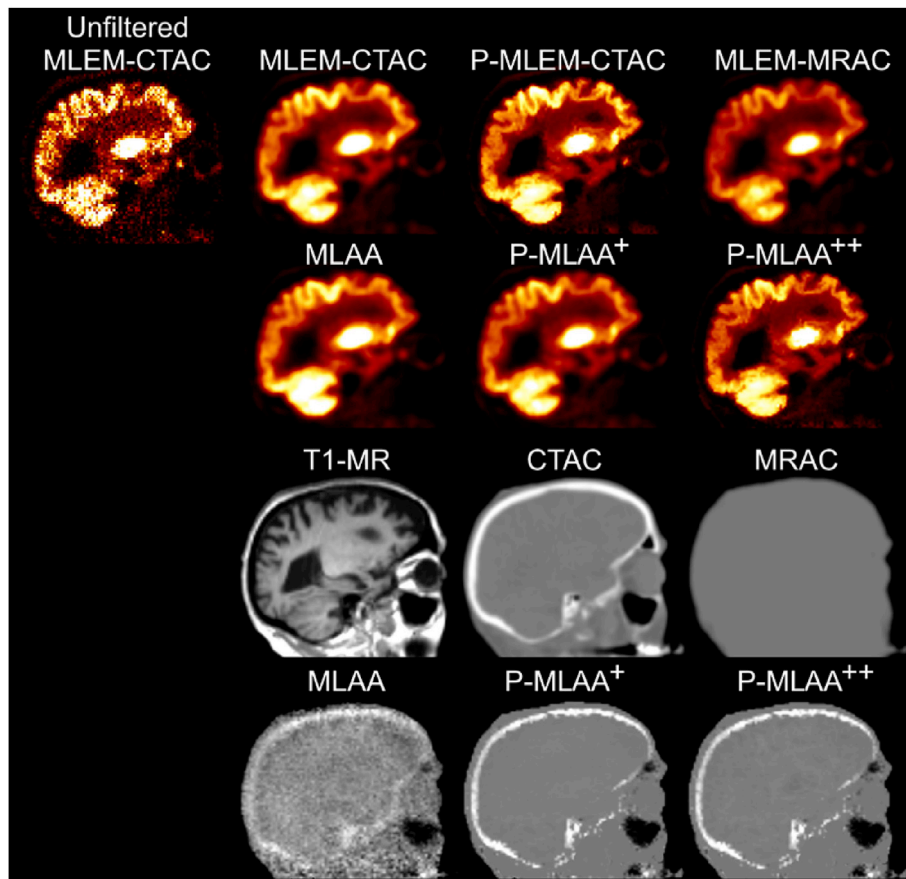


Figure 5. Same as Fig. 4 for another clinical FDG brain PET scan.

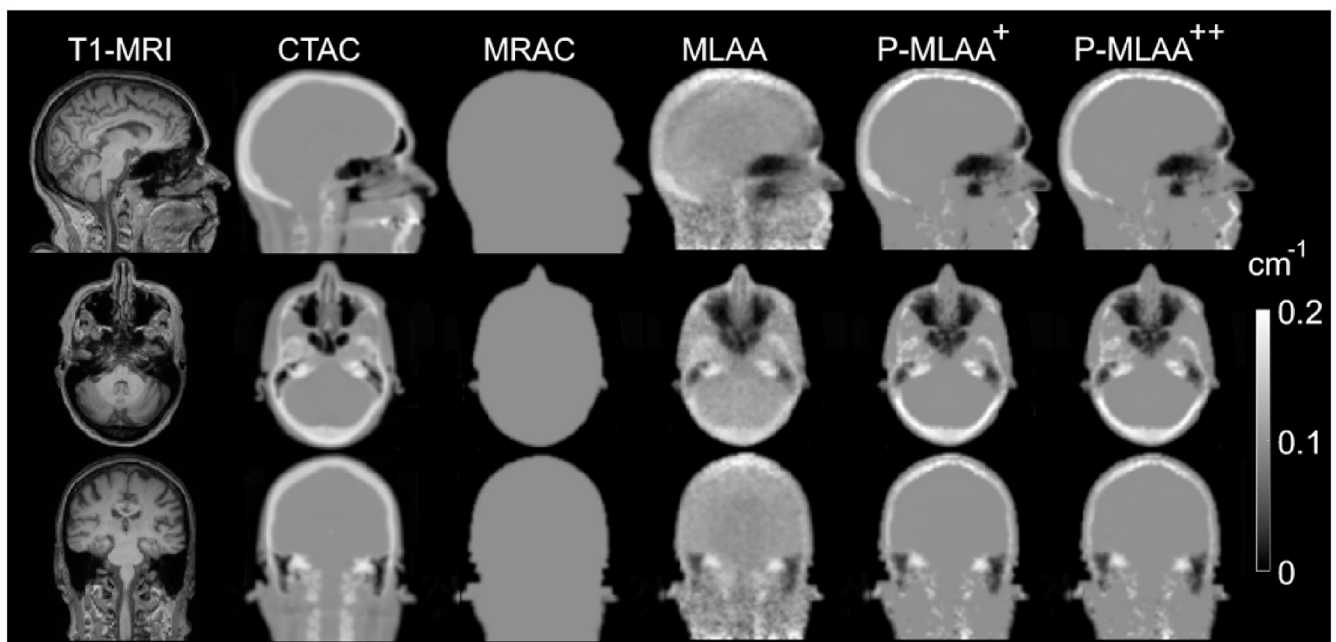


Figure 6. Comparison of the attenuation maps of the FDG brain PET study shown in Fig. 4, in sagittal, transverse and coronal views.

air cavities. However, it is noticeable that the MLAA algorithm has resulted in more than 8% overestimation errors in the cerebellum of the reconstructed PET images. The results showed that overall the MLEM-MRAC, P-MLEM-MRAC, MLAA, P-MLAA⁺ and P-MLAA⁺⁺ algorithms

led to -13.5 ± 3.1 , -13.4 ± 3.1 , -2.0 ± 6.5 , -3.0 ± 3.5 and $-4.2 \pm 3.6\%$ errors, respectively. The MLAA algorithm achieved lower mean errors but a higher standard deviation of the errors. The root sum of squares (RSS) of the errors, which includes both mean and variance, showed that

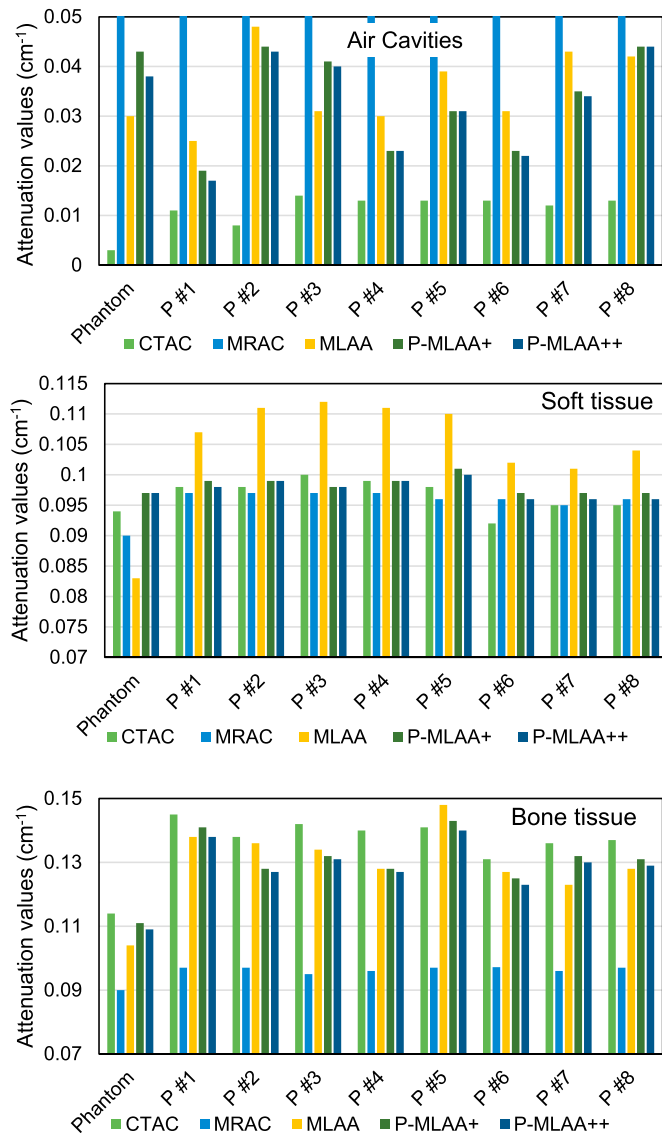


Figure 7. Mean attenuation values of air cavities, soft tissue and bone calculated for the brain phantom and patient datasets using the studied AC methods.

the above methods result in 13.8, 13.7, 6.8, 4.6 and 5.6% RSS error.

Fig. 10 shows the scatter plots of activity in 14 ROIs of the PET images

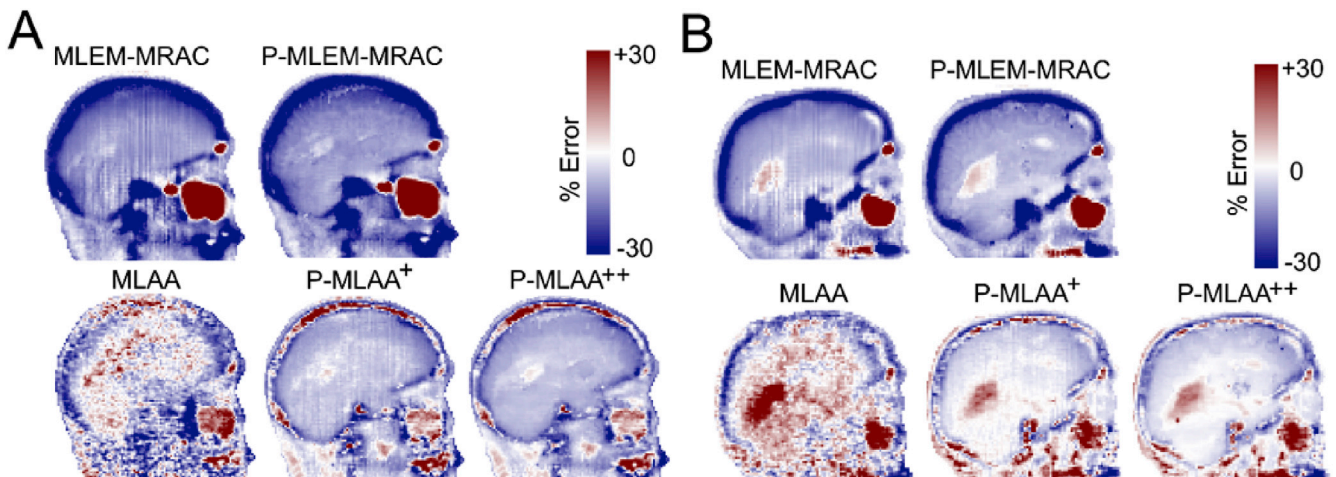


Figure 8. The voxel-wise error maps of the reconstructed PET images of the patient datasets shown in (A) Fig. 3 and (B) Fig. 4.

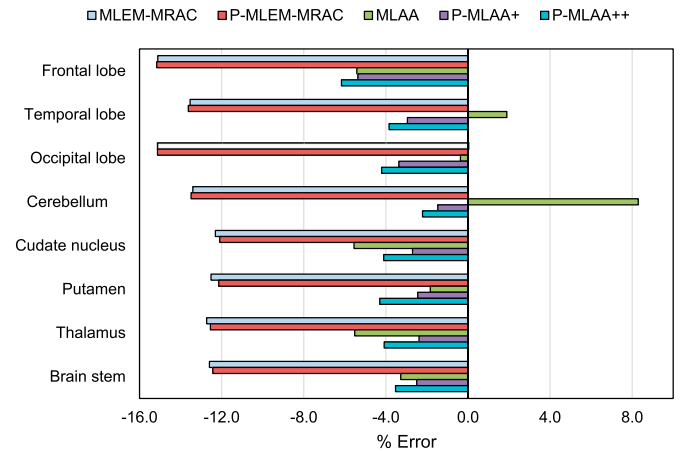


Figure 9. Mean of PET quantification errors in 8 brain regions calculated over all patients for the different AC methods with respect to reference MLEM-CTAC and P-MLEM-CTAC methods.

of all 8 clinical datasets reconstructed using different algorithms versus their reference PET images reconstructed using MLEM-CTAC and P-MLEM-CTAC algorithms. The figure also presents the linear regression plots illustrating the correlation between the tracer uptakes. The results show that the PET uptake values of the P-MLAA⁺ and P-MLAA⁺⁺ algorithms are highly correlated to CTAC PET values over all brain regions with $R^2 = 0.987$ and $R^2 = 0.984$, respectively. The regression lines showed that the MRAC method achieves the lowest R^2 of 0.944 and a regression line with slope of lower than one due to tracer uptake underestimations.

4. Discussion

With introduction of simultaneous PET-MR scanners in clinical practice, the development and evaluation of novel reconstruction methods that exploit MRI anatomical information for improving PET image quality and quantitative accuracy are of high importance. In this study, we proposed a joint PET activity and attenuation reconstruction algorithms that combines the efforts directed toward MR-guided PET partial volume and attenuation correction using state-of-the-art reconstruction algorithms, where MRI anatomical information is used to improve both activity reconstruction and emission-based attenuation estimation.

Our simulation results showed that our proposed anato-functional penalty function effectively exploits both MRI and PET information in order to reduce noise in the PET images while preserving their

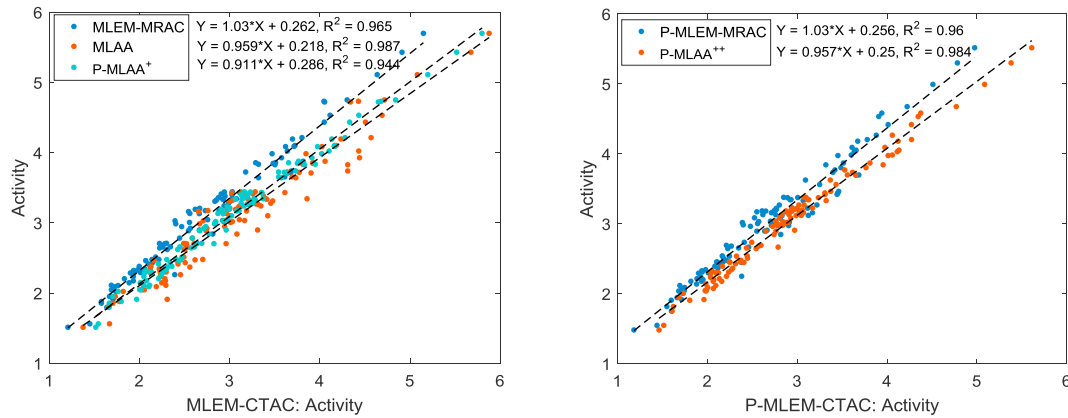


Figure 10. Scatter and linear regression plots between the tracer uptake in PET images reconstructed using reference MLEM-CTAC and P-MLEM-CTAC maps and those reconstructed using the different AC maps.

anatomical boundaries and unique lesions. In (Mehranian et al., 2017), we demonstrated that this penalty function can outperform state-of-the-art anatomical penalty functions that often rely on only T1-weighted MR images. The performance of this penalty function depends to a large extent on the selection of the bandwidth parameters, σ_λ and σ_θ , which control the shape of Gaussian similarity kernels used in the penalty function. In addition, due to differences in signal intensity of the PET and MR images, these parameters should be chosen appropriately with respect to the magnitude of the edges. Similarly, for different PET radiotracers and MR sequences, these parameters vary and need to be adjusted. As the MR images are reconstructed before the PET images, it is possible to perform the intensity normalization of each subject's MR to a reference MR with adjusted σ_θ . In our simulation and clinical data evaluation, we heuristically found these parameters for a few reconstructions and used the same parameters for all datasets as reported earlier. The results of attenuation map estimation showed that the application of the soft tissue preference penalty function can effectively reduce noise, possible cross-talk artifacts and the scaling of the reconstructed attenuation and activity maps. However, the regularization parameter, γ , of this penalty function should be chosen high enough in order to penalize the large deviations of the estimated soft tissue μ -values from their expected value. In (Mehranian and Zaidi, 2015b), we showed that as γ goes to zero the proposed algorithm reduces to the MLAA algorithm.

The evaluation of the AC methods using the clinical datasets also demonstrated that the exclusion of the bone tissue in attenuation correction of brain PET data can significantly underestimate the tracer concentration, especially in the regions close to the bone. For the simulated dataset, the MLAA algorithm underestimated the soft tissue's attenuation values while for the clinical datasets, it showed an overestimation. This discrepancy can be attributed to the instability of the algorithm for different datasets. For the reconstruction of the simulated datasets, we used the same scatter sinograms that were added to true sinograms, therefore the scatter correction of the simulated datasets was perfect, however, for the clinical dataset, the contribution of the scatter coincidences is approximated using single scatter simulation (SSS) and their tail fitting to the prompts coincidences measured in the sinogram bins (or LORs) out of the patient's body contour. In addition, the SSS algorithm does not take into account the multiple scattering and more importantly out of field of view scatter coincidences. Therefore, the MLAA algorithm behaved differently for the clinical datasets. It is interesting to note that for our initial simulations without inclusion of scatters and randoms, the attenuation and activity maps reconstructed by this algorithms were free of scale and matched their true maps. As mentioned before, the MRAC maps were used for the estimation of the scatter sinograms used during MLAA and P-MLAA algorithms. In (Burgos et al., 2014b), it has been shown that there is a negligible difference

between the scatters simulated using UTE MR-segmentation based (which includes bones), atlas-registration based and CT-based AC methods. However, in this study, we noticed that the accurate segmentation of the MR images for the body contour is of high importance for accurate tail fitting of the simulated scatter sinograms. The reason is that the LORs outside of the body contour are usually identified from a sinogram mask obtained by the forward projection of the attenuation maps in which the scanner's bed has been removed. Therefore, if the body contour is under-segmented, the tail fitting and scaling of the simulated scatters will be substantially inaccurate, as the sinogram mask will also include the LORs passing through the subject's body, while over-segmenting the body contour will not result in significantly erroneous tail fitting. To avoid mis-registration between CT and T1-weighted MR images of the patients of our study, the contours of the soft tissue class of the MRAC maps were obtained from the segmentation of the CTAC maps using a simple thresholding. In supplemental materials Fig. 4, the impact of under-segmentation of the body contour on the scaling of scatter profiles has been shown. In a few cases for our clinical datasets, we noticed that thresholding of the CTAC map can lead to under-segmentation of the CTAC map, given their lower resolution and PVE at the air/soft tissue interfaces.

Our clinical results for eight patient datasets showed that the MRAC and P-MLAA⁺ algorithms lead to, on average, -13% and -3% quantification errors over different regions of the brain. Previously in (Mehranian et al., 2016a), we evaluated the quantitative performance of these methods with an atlas-based AC method using 14 patient datasets. It was found that the MRAC and the P-MLAA⁺ (in that study, named as MLAA-GMM) algorithms lead to, on average, -16% and -13% quantification errors over different regions of the brain. In that study the PET images were reconstructed by a clinical standard protocol which consisted of 3 iterations and 21 subsets and PSF resolution modelling. The attenuation maps of the P-MLAA⁺ algorithm were reconstructed using 120 updates. The resulting attenuation maps were then used for the clinical standard image reconstruction. While in this study, the activity images and attenuation maps were reconstructed in 200 and 300 updates, consistent among the studied reconstruction methods. Another reason for the improved results of the P-MLAA⁺ algorithm in this study is that the erroneous scatter estimations were corrected by improving the body contour of MRAC maps, as described above.

The results showed that despite of the fact that the MLAA algorithm overestimated the soft tissue attenuation values in the patient datasets considered, the average PET quantitative performance of the algorithm is far better than the MRAC method and close to the P-MLAA algorithms. This might be attributed to the fact that the impact of bone μ -value underestimated by this algorithm is counteracted by overestimated soft tissue μ -value. However, as a compromise the regional errors are increased and thus this algorithm showed higher variations in

quantification errors. It was also found that the P-MLAA⁺⁺ algorithm results in a slightly increased overall quantification error of 4% compared to the P-MLAA⁺ algorithm. As mentioned earlier, the incorporation of MRI anatomical information during PET image reconstruction would result in the propagation of noise and any mismatch between calculated and measured emission data into the attenuation map estimation step. Therefore, as seen in Fig. 5, the attenuation map for of P-MLAA⁺⁺ shows more noise and a trace of the activity (cross-talk artefact), which has eventually a slightly underestimated attenuation value (see Fig. 7) and therefore increased error in activity. In this study, we used the same regularization parameter, γ , of the employed tissue preference penalty function for both P-MLAA algorithms.

Since the joint reconstruction of attenuation activity depends on count level, activity distribution and TOF timing resolution, using MRI information to guide attenuation estimation is important for PET tracers that have localized uptake distributions (which thus do not match the spatial support of the attenuation map), as well as for the current clinical PET-MR scanners whose TOF timing resolution is at best around 400 ps (Levin et al., 2016). For instance, as shown in Supplemental Fig. 2, the MLAA algorithm results in high attenuation coefficients at the edge of the PET axial FOV (neck area), where the scanner's sensitivity and count level is lower. It is worth noting that for the case of dynamic PET studies with low count frames, a possible solution is to first estimate the attenuation maps from all data collected in a static PET scan, and then to use the estimated attenuation maps for the subsequent low-count dynamic frames. The activity distribution also impacts the accuracy of the estimated attenuation maps, as these emission-based methods rely on the attenuation experienced by the emission data. Therefore, for tracers with localized uptake, the success of these AC methods is questionable and needs further investigation.

This study has some limitations that need to be emphasized. The performance of the proposed emission-based AC methods was only compared with the conventional 2-class segmentation based AC method implemented on the Philips Ingenuity TF PET/MR system. However, for the case of brain PET-MR imaging, advanced atlas-registration based AC methods are going to be the method of choice in practice and, as such, the comparison with these AC methods still needs to be performed. Another limitation is the fact that the ground truth CTAC attenuation maps used for our simulations do not take the intra-class variability of attenuation coefficients into account, which renders the simulations less realistic and thus limits the validation of the AC methods. The performance of the

proposed MR-guided penalty function depends on the accurate identification of the soft tissue label, since any over-segmentation of soft tissue can suppress the derivation of bone or air μ -values. In this study, we derived this label using a simple thresholding. Thus, the regions of low MRI signal were identified as the regions complementing soft tissue and background air. However, some low-intensity regions might be mis-segmented as soft tissue. A more robust approach is the utilization and development of shape-based or multi-atlas segmentation techniques that shape and accurately identify soft tissues (Aljabar et al., 2009).

5. Conclusion

In this work, we proposed a joint activity and attenuation reconstruction method that exploits MR anatomical information for improving the quantitative accuracy of PET images by improved attenuation correction of PET data and at the same time robust partial volume correction of the reconstructed PET images. A novel anato-functional penalty function was employed to guide PET image reconstruction while a soft tissue preference penalty function was used for the estimation of attenuation maps. Our simulations and clinical results showed that the proposed joint reconstruction lead to improved quality PET images based on visual and quantitative evaluations in comparison with other attenuation correction techniques. It was found the studied joint reconstruction methods lead to less than 5% error in the PET quantification, while the 2-class MR-segmentation based method results in up to 13% errors. Future work would require the evaluation of the proposed method for non-FDG tracers with localized tracer uptake and for TOF PET-MRI scanners.

Conflict of interest

The authors declare no conflict of interest.

Acknowledgements

This work is supported by Engineering and Physical Sciences Research Council (EPSRC) under grant EP/M020142/1 and the Swiss Cancer Research Foundation under Grant KFS-3855-02-2016. According to EPSRC's policy framework on research data, all simulation and clinical results supporting this study are openly available at <https://doi.org/10.5281/zenodo.887913>.

Appendix A

In this study, we followed the alternative formulation of the Shannon joint entropy prior proposed in Appendix of (Somayajula et al., 2011) in which the Shannon joint entropy prior is approximated, which is effectively reduced to a joint Burg entropy (see Eq. 32 in the mentioned above reference).

The joint Burg entropy is defined as:

$$R(\lambda) = \frac{1}{N} \sum_j \log \left(\frac{1}{N} \sum_b \mathcal{F}(\lambda_j, \lambda_b, \sigma_\lambda) \mathcal{F}(\theta_j, \theta_b, \sigma_\theta) \right)$$

Its partial derivative is then given by:

$$\frac{\partial R(\lambda)}{\partial \lambda_j} = \frac{1}{N} \sum_b \frac{\mathcal{F}'(\lambda_j, \lambda_b, \sigma_\lambda) \mathcal{F}(\theta_j, \theta_b, \sigma_\theta)}{\sum_b \mathcal{F}(\lambda_j, \lambda_b, \sigma_\lambda) \mathcal{F}(\theta_j, \theta_b, \sigma_\theta)} + \frac{1}{N} \sum_b \frac{\mathcal{F}'(\lambda_b, \lambda_j, \sigma_\lambda) \mathcal{F}(\theta_b, \theta_j, \sigma_\theta)}{\sum_b \mathcal{F}(\lambda_b, \lambda_j, \sigma_\lambda) \mathcal{F}(\theta_b, \theta_j, \sigma_\theta)}$$

Given the symmetry of the terms, we would have

$$\frac{\partial R(\lambda)}{\partial \lambda_j} = \frac{2}{N} \sum_b \frac{\mathcal{F}'(\lambda_j, \lambda_b, \sigma_\lambda) \mathcal{F}(\theta_j, \theta_b, \sigma_\theta)}{\sum_b \mathcal{F}(\lambda_j, \lambda_b, \sigma_\lambda) \mathcal{F}(\theta_j, \theta_b, \sigma_\theta)} = \frac{2}{N\sigma_\lambda^2} \sum_b \frac{\mathcal{F}(\lambda_j, \lambda_b, \sigma_\lambda) \mathcal{F}(\theta_j, \theta_b, \sigma_\theta)}{\sum_b \mathcal{F}(\lambda_j, \lambda_b, \sigma_\lambda) \mathcal{F}(\theta_j, \theta_b, \sigma_\theta)} (\lambda_j - \lambda_b)$$

The above derivative was heuristically modified by evaluating the summation for the voxels that are in the neighbourhood of the j th voxel and by including the distance weighting coefficients ξ_{jb} , as follows:

$$\frac{\partial R(\lambda)}{\partial \lambda_j} = -2 \sum_{b \in \mathcal{J}_j} \xi_{jb} \omega_{jb} (\lambda_j - \lambda_b), \omega_{jb} = \frac{\mathcal{E}(\lambda_j, \lambda_b, \sigma_\lambda) \mathcal{E}(\theta_j, \theta_b, \sigma_\theta)}{\sum_b \mathcal{E}(\lambda_j, \lambda_b, \sigma_\lambda) \mathcal{E}(\theta_j, \theta_b, \sigma_\theta)}$$

which is similar to the derivative of a weighted quadratic penalty function with a local neighbourhood. In this study, we employed a one-step-late algorithm, which requires the evaluation of the derivative of the penalty function at previous image update.

Appendix B. Supplementary data

Supplementary data related to this article can be found at <http://dx.doi.org/10.1016/j.neuroimage.2017.09.006>.

References

- Aasheim, L.B., Karlberg, A., Goa, P.E., Haberg, A., Sorhaug, S., Fagerli, U.M., Eikenes, L., 2015. PET/MR brain imaging: evaluation of clinical UTE-based attenuation correction. *Eur. J. Nucl. Med. Mol. Imaging* 42, 1439–1446.
- Aljabar, P., Heckemann, R.A., Hammers, A., Hajnal, J.V., Rueckert, D., 2009. Multi-atlas based segmentation of brain images: atlas selection and its effect on accuracy. *Neuroimage* 46, 726–738.
- Arabi, H., Zaidi, H., 2016. One registration multi-atlas-based pseudo-CT generation for attenuation correction in PET/MRI. *Eur. J. Nucl. Med. Mol. Imaging* 43, 2021–2035.
- Bai, B., Li, Q., Leahy, R.M., 2013. Magnetic resonance-guided positron emission tomography image reconstruction. *Semin. Nucl. Med.* 43, 30–44.
- Bowsher, J.E., Hong, Y., Hedlund, L.W., Turkington, T.G., Akabani, G., Badea, A., Kurylo, W.C., Wheeler, C.T., Cofer, G.P., Dewhurst, M.W., Johnson, G.A., 2004. Utilizing MRI information to estimate F18-FDG distributions in rat flank tumors. In: *IEEE Nucl. Sci. Symp. Conf. Rec.*, Vol. 2484, pp. 2488–2492.
- Burgos, N., Cardoso, M.J., Thielemans, K., Modat, M., Pedemonte, S., Dickson, J., Barnes, A., Ahmed, R., Mahoney, C.J., Schott, J.M., Duncan, J.S., Atkinson, D., Arridge, S.R., Hutton, B.F., Ourselin, S., 2014a. Attenuation correction synthesis for hybrid PET-MR scanners: application to brain studies. *IEEE Trans. Med. Imaging* 33, 2332–2341.
- Burgos, N., Thielemans, K., Cardoso, M.J., Markiewicz, P., Jiao, J., Dickson, J., Duncan, J.S., Atkinson, D., Arridge, S.R., Hutton, B.F., Ourselin, S., 2014b. Effect of scatter correction when comparing attenuation maps: application to brain PET/MR. In: *2014 IEEE Nuclear Science Symposium and Medical Imaging Conference (NSS/MIC)*, pp. 1–5.
- Camey, J.P., Townsend, D.W., Rappoport, V., Bendriem, B., 2006. Method for transforming CT images for attenuation correction in PET/CT imaging. *Med. Phys.* 33, 976–983.
- Cocoso, C.A., Kollokian, V., Kwan, R.K.-S., Evans, A.C., 1997. BrainWeb: online interface to a 3D MRI simulated brain database. *Neuroimage* 5, S425.
- Defrise, M., Rezaei, A., Nuyts, J., 2012. Time-of-flight PET data determine the attenuation sinogram up to a constant. *Phys. Med. Biol.* 57, 885–899.
- Delso, G., Fürst, S., Jakoby, B., Ladebeck, R., Ganter, C., Nekolla, S.G., Schwaiger, M., Ziegler, S.I., 2011. Performance measurements of the Siemens mMR integrated whole-body PET/MR scanner. *J. Nucl. Med.* 52, 1914–1922.
- Green, P.J., 1990. Bayesian reconstructions from emission tomography data using a modified EM algorithm. *IEEE Trans. Med. Imaging* 9, 84–93.
- Hofmann, M., Bezrukov, I., Mantlik, F., Aschoff, P., Steinke, F., Beyer, T., Pichler, B.J., Schölkopf, B., 2011. MRI-based attenuation correction for whole-body PET/MRI: quantitative evaluation of segmentation- and atlas-based methods. *J. Nucl. Med.* 52, 1392–1399.
- Keereman, V., Fierens, Y., Broux, T., De Deene, Y., Lonnew, M., Vandenberghe, S., 2010. MRI-based attenuation correction for PET/MRI using ultrashort echo time sequences. *J. Nucl. Med.* 51, 812–818.
- Klein, S., Staring, M., Murphy, K., Viergever, M.A., Pluim, J.P., 2010. Elastix: a toolbox for intensity-based medical image registration. *IEEE Trans. Med. Imaging* 29, 196–205.
- Ladefoged, C.N., Law, I., Anazodo, U., St Lawrence, K., Izquierdo-Garcia, D., Catana, C., Burgos, N., Cardoso, M.J., Ourselin, S., Hutton, B., Merida, I., Costes, N., Hammers, A., Benoit, D., Holm, S., Juttukonda, M., An, H., Cabello, J., Lukas, M., Nekolla, S., Ziegler, S., Fenchel, M., Jakoby, B., Casey, M.E., Benzinger, T., Hojgaard, L., Hansen, A.E., Andersen, F.L., 2016. A multi-centre evaluation of eleven clinically feasible brain PET/MRI attenuation correction techniques using a large cohort of patients. *Neuroimage* 147, 346–359.
- Levin, C.S., Maramraju, S.H., Khalighi, M.M., Deller, T.W., Delso, G., Jansen, F., 2016. Design features and mutual compatibility studies of the time-of-flight PET capable GE SIGNA PET/MR system. *IEEE Trans. Med. Imaging* 35, 1907–1914.
- Martinez-Möller, A., Souvatzoglou, M., Delso, G., Bundschuh, R.A., Chefed'hotel, C., Ziegler, S.I., Navab, N., Schwaiger, M., Nekolla, S.G., 2009. Tissue classification as a potential approach for attenuation correction in whole-body PET/MRI: evaluation with PET/CT data. *J. Nucl. Med.* 50, 520–526.
- Mehranian, A., Arabi, H., Zaidi, H., 2016a. Quantitative analysis of MRI-guided attenuation correction techniques in time-of-flight brain PET/MRI. *Neuroimage* 130, 123–133.
- Mehranian, A., Arabi, H., Zaidi, H., 2016b. Vision 20/20: magnetic resonance imaging-guided attenuation correction in PET/MRI: challenges, solutions, and opportunities. *Med. Phys.* 43, 1130–1155.
- Mehranian, A., Belzunce, M.A., Niccolini, F., Politis, M., Prieto, C., Turkheimer, F., Alexander, H., Reader, A.J., 2017. PET image reconstruction using multi-parametric anato-functional priors. *Phys. Med. Biol.* 62 (15), 5975–6007.
- Mehranian, A., Zaidi, H., 2015a. Clinical assessment of emission- and segmentation-based MR-guided attenuation correction in whole-body time-of-flight PET/MR imaging. *J. Nucl. Med.* 56, 877–883.
- Mehranian, A., Zaidi, H., 2015b. Joint estimation of activity and attenuation in whole-body TOF PET/MRI using constrained Gaussian mixture models. *IEEE Trans. Med. Imaging* 34, 1808–1821.
- Rezaei, A., Defrise, M., Bal, G., Michel, C., Conti, M., Watson, C., Nuyts, J., 2012. Simultaneous reconstruction of activity and attenuation in Time-of-Flight PET. *IEEE Trans. Med. Imaging* 31, 2224–2233.
- Salomon, A., Goedicke, A., Schweizer, B., Aach, T., Schulz, V., 2011. Simultaneous reconstruction of activity and attenuation for PET/MR. *IEEE Trans. Med. Imaging* 30, 804–813.
- Sekine, T., Buck, A., Delso, G., Ter Voert, E.E., Huellner, M., Veit-Haibach, P., Warnock, G., 2016a. Evaluation of atlas-based attenuation correction for integrated PET/MR in human brain: application of a head atlas and comparison to true CT-based attenuation correction. *J. Nucl. Med.* 57, 215–220.
- Sekine, T., Ter Voert, E.E., Warnock, G., Buck, A., Huellner, M.W., Veit-Haibach, P., Delso, G., 2016b. Clinical evaluation of ZTE attenuation correction for brain FDG-PET/MR imaging-comparison with atlas attenuation correction. *J. Nucl. Med.* 57 (12), 1927–1932.
- Somayajula, S., Panagiotou, C., Rangarajan, A., Li, Q., Arridge, S.R., Leahy, R.M., 2011. PET image reconstruction using information theoretic anatomical priors. *IEEE Trans. Med. Imaging* 30, 537–549.
- Vunckx, K., Atré, A., Baete, K., Reilhac, A., Deroose, C.M., Van Laere, K., Nuyts, J., 2012. Evaluation of three MRI-based anatomical priors for quantitative PET brain imaging. *IEEE Trans. Med. Imaging* 31, 599–612.
- Wiesinger, F., Sacolick, L.L., Menini, A., Kaushik, S.S., Ahn, S., Veit-Haibach, P., Delso, G., Shanbhag, D.D., 2016. Zero TE MR bone imaging in the head. *Magn. Reson. Med.* 75, 107–114.
- Zaidi, H., Becker, M., 2016. The promise of hybrid PET-MRI: technical advances and clinical applications. *IEEE Sign. Proc. Mag.* 33, 67–85.
- Zaidi, H., Montandon, M.L., Slosman, D.O., 2003. Magnetic resonance imaging-guided attenuation and scatter corrections in three-dimensional brain positron emission tomography. *Med. Phys.* 30, 937–948.